J. Appl. Comput. Mech., 7(1) (2021) 135-147
DOI: 10.22055/JACM.2020.34843.2480

ISSN: 2383-4536
jacm.scu.ac.ir

Shahid Chamran University of Ahvaz

Journal of Applied and Computational Mechanics

Research Paper

Forced Response of a Low-Pressure Turbine Blade using Spectral/hp Element Method: Direct Numerical Simulation

Daniel H. Wacks[1], M. E. Nakhchi[2], M. Rahmati[3]

[1] Department of Mechanical & Construction Engineering, Northumbria University, Newcastle upon Tyne, NE1 8ST, UK, Email: Daniel.wacks@northumbria.ac.uk

[2] Department of Mechanical & Construction Engineering, Northumbria University, Newcastle upon Tyne, NE1 8ST, UK, Email: mahdi.nakhchi@northumbria.ac.uk

[3] Department of Mechanical & Construction Engineering, Northumbria University, Newcastle upon Tyne, NE1 8ST, UK, Email: mohammad.rahmati@northumbria.ac.uk

Received August 31 2020; Revised September 16 2020; Accepted for publication September 23 2020.
Corresponding author: M. E. Nakhchi (mahdi.nakhchi@northumbria.ac.uk)

Abstract. The Spectral/HP element method has been applied to perform Direct Numerical Simulations (DNS) over a single T106A turbine blade-row using the open source software Nektar++. The main goal of the current study is to perform preliminary investigations at modest Reynolds and Mach numbers, 8000 and 0.1 respectively, for uniform, steady flow past the aerofoil by employing Nektar++'s solver for the 2D Navier-Stokes equations for incompressible flow. The mesh was firstly validated against results obtained using the same software and for a similar set of parameter values. One dimensional, pitch-wise harmonic vibrations were subsequently imposed on the blade by means of a coordinate transformation. A parametric study in terms of the frequency and amplitude of the vibrations was carried out. The effects of the vibrations on entire domain, along the blade surface and in its wake were assessed. The pressure on the blade surface and the wake loss were each decomposed into components arising due to the mean flow and due to the vibrations. In each case the dominant components were then identified for the values of frequency and amplitude considered here.

Keywords: DNS; Spectral/hp element method; Low-pressure turbine; Blade vibrations.

1. Introduction

The unsteady flow of air through successive blade rows of a gas turbine engine can often influence the dynamic structure behavior of the blades. These fluid-structure interactions can give rise to complex, two-way, aero-elastic phenomena in which energy is transferred from the main stream to the structure and vice-versa, which may lead to the growth of the vibration amplitude and eventually to structural failure. The majority of flight time for low pressure turbines (LPTs) is spent at high altitudes, where low air density results in low Reynolds numbers which are prone to separation and transition effects due to the adverse pressure gradient present on the suction surface of the blade [1]. A significant amount of research and effort was devoted to improve the efficiency of LPTs [2] and high levels of efficiency (90-93%) have since been attained. Focus has now shifted towards reducing weight and manufacturing costs, without compromising on high levels of efficiency [3]. 'High-lift' blade designs, in which the aerodynamic loading on each blade is increased significantly [4], ensure that the required stage loading is achieved with fewer blades, thereby reducing the total weight of the engine. These design goals decrease flutter in LPTs [5] and attain higher per-stage loading conditions and shock structures [6]. Izadpanah et al. [7] numerically investigated the fluid flow over oscillating blade in a straight channel. They concluded that in most cases the effects of the oscillation angles are higher than the oscillating velocity on thermal performance enhancement. Evaluating the effects of the geometrical parameters on the performance of the other turbines, such as wind turbines [8, 9] and vertical axis turbines [10] revealed that appropriate design of the blades play important role in aerodynamic designs.

Crack initiation and propagation and destructive failure depend on the type of excitation (forced or self-excited) experienced by the blade [11] and accurate prediction of flutter and forced response in turbomachines remains one of the greatest unsolved challenges for the industry [12]. Much effort has been made over the past two decades to seek efficient numerical approaches for turbomachinery aeromechanical analysis and design with various fidelity levels. Conventional time-linearized harmonic methods often exhibit solution divergence for separated flows and, hence, such techniques would be inadequate for modelling flow through modern LPTs where flow separation is inevitable. Aerodynamic damping calculations have been performed using frequency domain methods in an isolated rotor row. However, it has been shown by Silcowski & Hall [13] that multistage effects can have a significant impact on the middle blade-row rotor aerodynamic damping due to the acoustic upstream mode from the rotor onto the stator being reflected back onto the rotor with the same frequency as the stator wake. Therefore, a fully coupled, multi-row analysis is required for more accurate flutter predictions than the isolated blade-row case. Shams et al. [14] evaluated the torsional aeroelasticity of a wind turbine blade by using a new aerodynamic method at different Reynolds numbers. They concluded that the presence of static stall makes the amount of torsion smaller. The effects of different attack angles were also examined by them.

Published online: September 24 2020

Many numerical and experimental investigations are done in recent years for optimizing various turbine geometries [15, 16]. It was deduced that the unsteadiness flow structure over the blades has significant impact on the performance improvement of the turbines. Besides, Bovand et al. [17], and Rashidi et al. [18] showed that estimating the wake structure and flow separating point over aerodynamic objects, such as turbine blades and bluff bodies, can help to control the flow over the structure. Recent review article of Rashidi et al. [19] suggested that accurate prediction of the wake structures, flow unsteadiness [20], and vortex flows over the oscillating surfaces in essential in both aerodynamic and hydrodynamic applications. In summary, various sources of unsteadiness (see Fig. 1) such as wakes, multi-stage effects and pressure loadings can influence flutter and forced response in turbomachinery. However, very little is known about how the various sources of unsteadiness influence aero-elastic stability of turbomachinery blades. Whilst the long-term goals are to gain an understanding of all of the aforementioned sources of unsteadiness by performing suitable parametric analyses employing high-fidelity 3-dimensional Direct Numerical Simulations (DNS) of multiple blade-rows in order to be able to optimize efficiency, aerodynamic loading and weight, the immediate goals of the current paper are more modest: to utilize DNS to perform a parametric study of the forced-response of a 2-dimensional LPT blade cross-section. Experience gained in the analysis of low Reynolds and Mach number cases and incompressible flow will assist future studies where more realistic conditions are considered, which will be followed by studies of multiple fully 3-dimensional blade-rows.

The novelty of this approach is two-fold: firstly, in its application of low polynomial order h-type solvers as well as higher p-order piecewise polynomial order solvers in the form on the Nektar++ code to the study of turbomachinery, where previous DNS studies of turbomachinery have been based on the harmonic balance methods [21] and phase solution methods [22-24], and, secondly, in that it presents the opportunity to undertake a pioneering study on the effect of vibrations on modern 'high-lift' LPTs. As a result of this the study should be considered significant in two ways. Firstly, there is a lack of experimental data which study the mechanism of interactions between transient flows, blade structures and aero-elastic instabilities in modern LPTs. This is in part due to the difficulty associated with obtaining such data experimentally. Secondly, this study will act as a benchmark against which low-fidelity codes may be compared.

2. Physical Description

Before beginning a discussion of the results obtained, we firstly describe the flow geometry and mesh used to perform the Direct Numerical Simulations and the boundary and initial conditions which were applied to these simulations. The T106A low-pressure turbine cascade has been studied extensively both in experiments [1], and numerical simulations [25, 26].The T106A profile represents the mid-span of the Pratt and Whitney PW2037 rotor airfoil [27]. The geometrical details are shown in table 1 and the blade geometry is illustrated in Fig. 2.

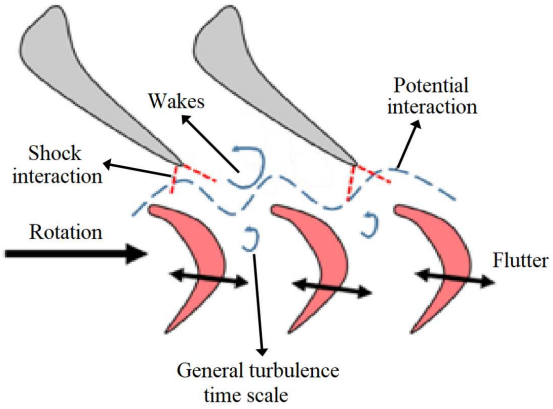

Fig. 1. Schematic view of the flow structure in T106 LPT stage.

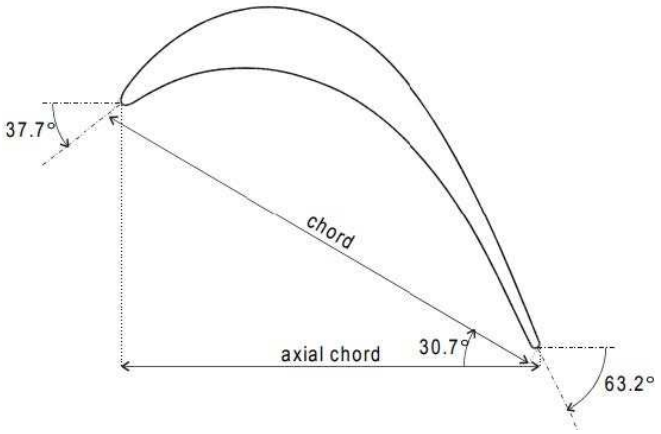

Fig. 2. Geometrical parameters Geometrical parameters of T106A low-pressure blade.

Table 1. T106A low-pressure blade cascade specifications.

Geometrical parameter	Value
Chord length (C)	1000mm
Axial chord length (L)	859mm
Pitch (P)	798mm
Span	1894mm
Suction surface length	1337mm
Pressure surface length	1162mm
Design exit flow angle	63.2°
Blade stagger	30.7°
Inlet flow angle	37.7°

Table 2. Turbulent flow parameters over LPT blade.

Flow parameter	Value
Ma	0.1
Re	8000
Pr	0.72
u_{ref}	34.3 ms^{-1}
p_{ref}	0 Pa
ρ_{ref}	1.225 kgm^{-3}

The mid-span section of a single passage of the cascade is meshed, using periodic boundary conditions both in the pitch and span directions. Upstream wakes are neglected, allowing for a clean, steady flow condition to be implemented at the inlet. In practical terms, both x- and y components of velocity are imposed explicitly (Dirichlet condition) and the gradient of the pressure (Neumann condition) at the inlet. The reverse holds true for the outlet: the pressure is subject to a Dirichlet condition and the velocity components to Neumann conditions. The computational domain consists of a mixed mesh such that the majority of the domain consists of triangular elements, whereas the boundary layer is made up of quadrilateral elements.

As has been mentioned at the end of Section 1, this preliminary investigation is limited to low Mach and low Reynolds number cases, allowing the approximation of incompressible flow. The Reynolds number is primarily limited to cases for which Re=8000, with comparison in the case of a stationary blade made to cases of Re=60,000. Parameter values pertaining to this flow are shown in table 2, where it should be noted that the velocity, u_{ref}, is incident to the inlet at the inlet flow angle, α = 37.7°, such that x- and y-velocity components $(u,v) = (u_{ref}\cos\alpha, u_{ref}\sin\alpha)$. Subsequent simulations, such as those for higher Reynolds numbers or those which incorporate blade vibrations, took the output of lower Reynolds number, stationary blade simulations as their initial condition.

3. Mathematical Formulation

3.1 Governing Equations

The two-dimensional incompressible Navier-Stokes (N-S) equations in a two-dimensional Cartesian domain, Ω, can be written as[28]:

$$\nabla.\mathrm{U} = 0 \tag{1}$$

$$\frac{\partial \mathrm{U}}{\partial \mathrm{t}} + \mathrm{U}.\nabla\mathrm{U} = -\nabla\mathrm{P} + \frac{1}{\mathrm{Re}}\nabla^2\mathrm{U} \tag{2}$$

where $\mathrm{U} = (u,v)$ is the fluid velocity in the x- and y-directions, respectively, P is the pressure and ν is the kinematic viscosity. Nektar++ uses a discontinuous spectral-hp element method, which combines both h- and p-type refinements (i.e. partitioning of the computational domain into separate elements together with spectral resolution within each element). Convergence is achieved by refining the mesh and/or increasing the polynomial order of the approximation. Nektar++'s incompressible flow solver allows one to solve the incompressible N-S equations by means of the Velocity Correction Scheme in which the velocity and pressure systems are decoupled. This splitting scheme is chosen due to its numerical efficiency. Of particular importance in the current study is Nektar++'s ability to simulate a moving body (e.g. a vibrating aerofoil blade) by imposing a forcing term. This allows one to solve the interaction system of an incompressible fluid flowing past flexible moving bodies without the difficulty and computational expense involved in a moving mesh. Body-fitted coordinates are employed so that an additional acceleration term (i.e. forcing term) is introduced to the momentum equations by the non-inertial transform from the deformed and moving coordinate system to the non-deformed and stationary one. Although several types of forcing are possible, the one that is utilized for the current study is the forced type, in which the vibration profiles of the moving body are specified by a given function. For the present work the vibration is limited to a single direction as specified in the next sections. Further details of the mathematical background and numerical implementation upon which the open-source spectral/hp-element code Nektar++ can be found in [29, 30].Details of the implementation of the vibration by means of coordinate transformation in Nektar++ can be found in Bao et al. [31, 32]. It is worth pointing out that similar numerical studies employing the finite element method and using a body-fitting coordinate transformation have been used to investigate the effects of flow-induced vibrations past a vibrating cylinder.

Table 3. Mesh and boundary layer conditions.

Parameters	Parameter symbols	Values
Mesh size at outer boundary	Δs_{outer}	0.05
Mesh size adjacent to BL	Δs_{inner}	0.002
Number of BL layers	N_{BL}	4.0
BL progression ratio	h_2/h_1	1.1
BL mesh size normal to blade	Δy (mm)	0.0017
BL mesh size tangent to blade	Δx (mm)	0.002

3.2 Mesh Generation and Forced Response Analysis

The mesh and boundary layer (BL) parameters have the values shown in table 3. The spatial resolution near the wall satisfies the following conditions:

$$\Delta x^{+}_{wall} = \frac{\Delta x}{\delta_v P} < 20, \quad \Delta y^{+}_{wall} = \frac{\Delta y}{\delta_v P} < 10 \tag{3}$$

where P is the polynomial order of the expansion basis and Δx and Δy are the wall spacing of the mesh in the tangential and normal directions to the blade surface respectively. The viscous length scale δ_v is calculated at each point of the blade by evaluating the local shear stress along the blade:

$$\delta_v = \nu \times \sqrt{\frac{\rho}{\tau_w}} \tag{4}$$

Finally, forced-response vibrations are imposed on the blade allowing movement in the y-direction alone. The blade oscillates about a fixed position with frequency, f, and amplitude, A, such that the coordinates of the blade are $(x,y) = (x_{i,0}, y_{i,0} + A\cos(\omega t))$ and the components of the vibrational velocity are $(u', v') = (0, -\omega A \sin(\omega t))$ where $(x_{i,0}, y_{i,0})$ are the set of points which describe the surface of the blade at time $t = 0$ and $\omega = 2\pi f$ is the angular frequency. The range of values for the frequency and amplitude which were chosen for this initial investigation of the effects of forced-response vibrations are: f = {100,200,400} and A/C varied between 0.001-0.1.

For the purpose of analyzing the resulting data and comparing with the harmonic balance and phase solution methods [22, 23] the velocity in the x- and y-directions and the pressure may be decomposed into the components which arise due to the background flow field and due to the vibration of the blade, such that:

$$Q = \overline{Q} + \tilde{Q}_A \cos(\omega t) + \tilde{Q}_B \sin(\omega t) \tag{5}$$

For Q={u,v,p}, where $\overline{Q}$ represents the component of Q arising due to the flow field and $\tilde{Q}_A$, and $\tilde{Q}_B$ represent the components arising due to the vibration of the blade. These parameters may be determined by solving the set of linear equations formed by considering Q at any 3 times during a single period of the vibration.

4. Results and Discussions

The instantaneous pressure and vorticity fields for the case of a single row of stationary T106A blades at Re=8000 and Re=60,000 are shown in Fig. 3. The maximum pressure value obtained throughout the whole domain pressure fields was approximately constant for both cases, but the magnitude of the minimum value increased by 50% for the higher Reynolds number case. The pressure in the immediate vicinity of the blade does not show any visible difference between the two cases (see also discussion of Fig. 5). Although the downstream pressure fields in both cases are predominantly negative or of low positive values, in the Re=8000 case a clear pattern of low pressure regions is visible, whereas in the Re=60,000 case there is far greater disorder of such regions. The instantaneous vorticity fields exhibit even more marked differences between the two cases. Firstly, the boundary layer region in the lower Reynolds number case appears significantly thicker than in the higher Reynolds number case. Secondly, there is clear separation of the boundary layer in the lower Reynolds number case towards the trailing edge of the blade, which is not apparent at all in the higher Reynolds number case. Finally, the vortical structures exhibited by the Re=8000 case show much more regularity than those exhibited by the Re=60,000 case: the areas of positive and negative vorticity are well-defined at the lower Reynolds number, but show considerable intermittency at the higher Reynolds number. It is worth noting that the ranges of both the pressure and the vorticity values in the color bars in both cases have been limited to allow for easier comparison.

Validation of the mesh used to obtain the instantaneous fields shown in Fig. 3 was obtained by considering the similar case which was investigated by Wissink [26] for which α=45.5° and Re=51,831. Good comparison was found for the velocity ratio given by Wissink as 1.57 and obtained using the current mesh to be 1.54. The wall static-pressure coefficient, $c_p = (p - \overline{p}_{out}) / (p_{in} - \overline{p}_{out})$, as given by Wissink was also compared and the results are shown in Fig. 4. The mean value of the pressure at the outlet was used for the parameter $\overline{p}_{out}$ and it was found that best fit was obtained when taking $u_{ref} = u_{out}$. With these parameter values, both pressure and suction surfaces show good qualitative fits, although quantitatively the pressure surface of the blade is a better fit than the suction surface.

The instantaneous fields shown in Fig. 3 were obtained by allowing the initial conditions to evolve until the total kinetic energy (KE) of the system assumed an approximately constant value. The temporal evolution of the kinetic energy (KE/KE_0), where KE_0 is the initial kinetic energy of the system, is shown in Fig. 5 (top) as a function of the normalized time (t/t_C), where $t_C = L/u_{ref}$ is the equivalent chord length (i.e. one equivalent chord length is the time taken for the mean flow to travel the length of the aerofoil). The normalized kinetic energy can be seen to attain a value of 2.0 at t/t_C =2.0, after which time it remains approximately constant.

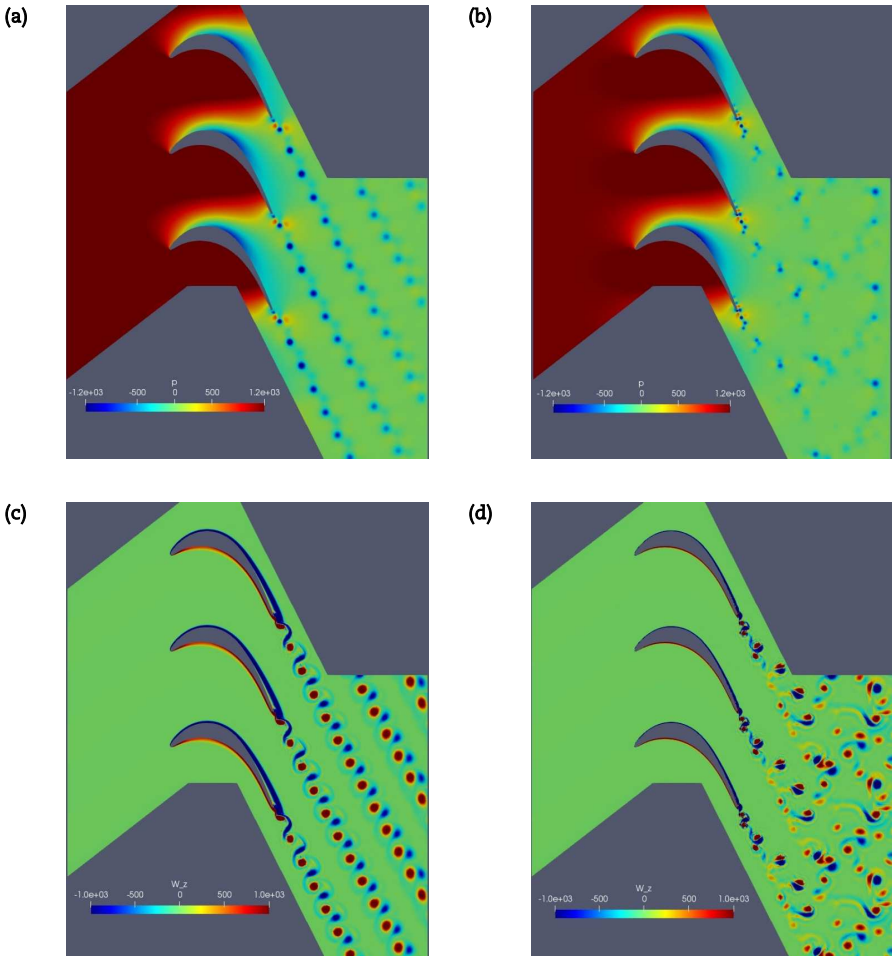

Fig. 3. Instantaneous (top) pressure and (bottom) vorticity fields for a single row of stationary T106A blades for the cases (left) $Re = 8000$ and (right) $Re = 60{,}000$. The same ranges for pressure and vorticity, respectively, have been used in both cases and have been centered at zero.

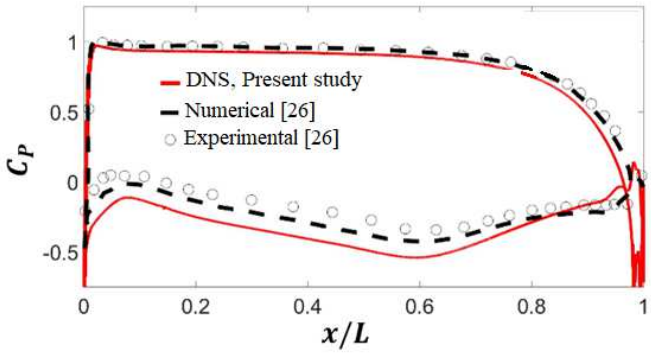

Fig. 4. validation of pressure coefficient, C_P, over a stationary LPT blade with Re = 51,831 and $\alpha = 45.5°$ with previous numerical and experimental studies [26].

The variation of the pressure coefficient, along the surface of the blade for Re=8000 obtained using the current mesh is shown in Fig. 5 (middle) and the results for the higher Reynolds number case (Re=60,000) were compared to those of the lower Reynolds number case and were found to coincide along almost the entire surface of the aerofoil with the exception of a small region near the trailing edge on the suction surface of the blade for which the pressure coefficient is greater in the Re=8000 case. Fig. 5 (bottom) also shows the variation of the wake loss, $w_e = (p\text{-}p_{inlet})/(1/2\ \rho_{ref}\ u^2_{ref})$, in the pitch direction. The wake loss has been evaluated at a location 0.35C downstream of the trailing edge which coincides with localized regions of low pressure in both the Re=8000 and Re=60,000 cases. The profiles for wake loss shown in Fig. 5 show that, although the same qualitative results persist in both cases, the magnitude of the wake loss is consistently lower for the higher Reynolds number case across the entire pitch direction. It can be seen that two peak points are detected in the wake profile over the LPT blade at both Re=8000 and 60,000. This is mainly due to the vortex generations over the blade for different Reynolds numbers. It can be seen that the maximum value of w_e=2.41 could be achieved for Re=60,000 at pitch ratio of 0.77.

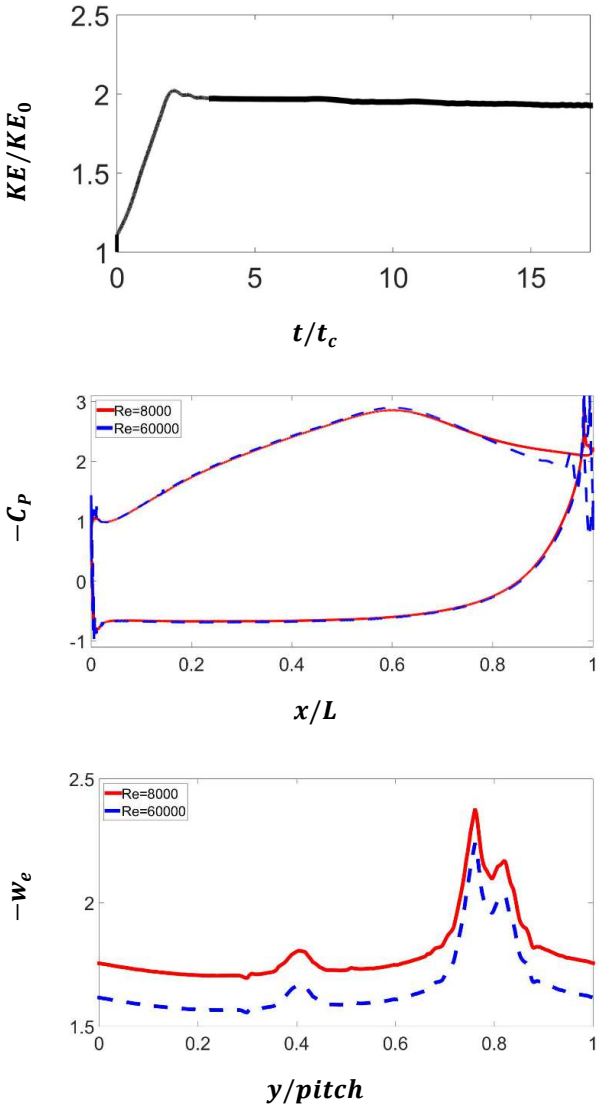

Fig. 5. (Top) Variation of total normalized kinetic energy, KE/KE_0, with normalised time, t/t_c, for a single stationary T106A blade for the case $Re = 8000$. Variation of (middle) pressure coefficient, $-C_P$, over the surface of a stationary T106A blade and (bottom) wake losses, $-w_e$, at a distance $0.35C$ downstream of the trailing edge of the blade for the cases (red solid line) $Re = 8000$ and (blue dashed line) $Re = 60\,000$.

Forced-response vibrations were introduced at this point and were allowed to develop fully over a time equivalent to $t=4T_v$, where $T_v=1/f$. The instantaneous fields were produced after this time had elapsed, whereas mean and fluctuating data were calculated based on 3 snapshots taken within the fourth and final time period of the vibration, namely: $\omega t=\pi,1.8\pi,2\pi$. The parametric investigation of the vibrations consisted of three frequencies, f=100,200,400, and different amplitudes, to allow for both the effects of increasing frequency and amplitude to be observed and analyzed. Fig. 6(i-ii) show the instantaneous pressure and vorticity fields respectively in the immediate vicinity of a single vibrating T106A blade out of the blade row. Only the larger 2 amplitudes are shown for each frequency of vibration since these cases exhibit the most significant vibration-based effects. Although the maximum magnitude of the pressure fields increases both with increasing frequency and amplitude, all sub-figures in Fig. 6(i) have been centered at zero to enable some degree of comparison between different cases. As such, it is readily apparent that the region upstream of the blade in each case remains largely positive in terms of pressure and the region downstream remains of negligible magnitude (i.e. close to zero). It is also clear that locations of low or negative pressure, corresponding to vortical structures (see Fig. 6(ii)), have developed in the vicinity of both the leading and trailing edges. The size and magnitude of these regions increase with increasing frequency and amplitude, although the effect of increasing amplitude appears more significant than that of increasing frequency, for the values considered in this study. In addition to this, the distance upstream of the leading edge which is inhabited by these locations of low or negative pressure increases both with frequency and amplitude.

A similar approach was adopted for the visualization of the instantaneous vorticity fields in Fig. 6(ii), although in this instance, besides centering the color scale at zero, the same magnitude was adopted for all cases. In this figure remnants of the organized vortical structures visible in Fig. 3(c) persist in the region of the outlet for some cases (see Fig. 6(ii) c-f). However, in the vicinity of both the leading and trailing edges vortical structures of larger magnitude, and sometimes diameter, have developed. As in the case of the pressure fields, these structures increase in size and magnitude with both increasing frequency and amplitude, and the effect of increasing amplitude is more apparent than that of increasing frequency for the values of the parameters considered here. Also, the distance upstream to which the vortical structures extend increases in most cases with both increasing frequency and amplitude. Furthermore, there is a noticeable region of negative vorticity in the immediate vicinity of the suction surface. This region remains well-behaved for the lower amplitude vibrations at all frequencies, 'hugging' the upper surface of the blade and remaining of consistent thickness but exhibits far more volatile behavior for the higher amplitude vibrations.

The temporal variation of the vortical structures is considered in the context of a single period of oscillation of the blade. Starting from a location near to the apex of its vibration (ωt=0.4π), the blade moves to locations near to its lowest position (ωt=0.8π,1.2π). The sub-figures show that near the apex position the vorticity along both surfaces of the blade in the vicinity of the trailing edge is predominantly positive, although the vorticity layer is thicker on the pressure side than on the suction side. Adjacent to the layer on the suction side near the trailing edge is a small region of negative vorticity. As the blade moves downwards under the effect of the vibration the small region of negative vorticity diminishes in size and strength, as does the positive vorticity layer along the suction surface – the positive vorticity layer along the pressure surface remains largely unaffected by the effects of the vibration. As the positive vorticity layer along the suction surface reduces in strength and width, a negative vorticity layer develops near to the trailing edge, which appears to 'creeps' further along the suction surface of the blade, until it has replaced the positive vorticity layer for as far as can be seen in these figures. This development accompanies the formation of a new vortex near to the trailing edge, which is shed as the blade returns to its apex position and at which point in time a new thin positive vorticity layer has formed along the suction surface.

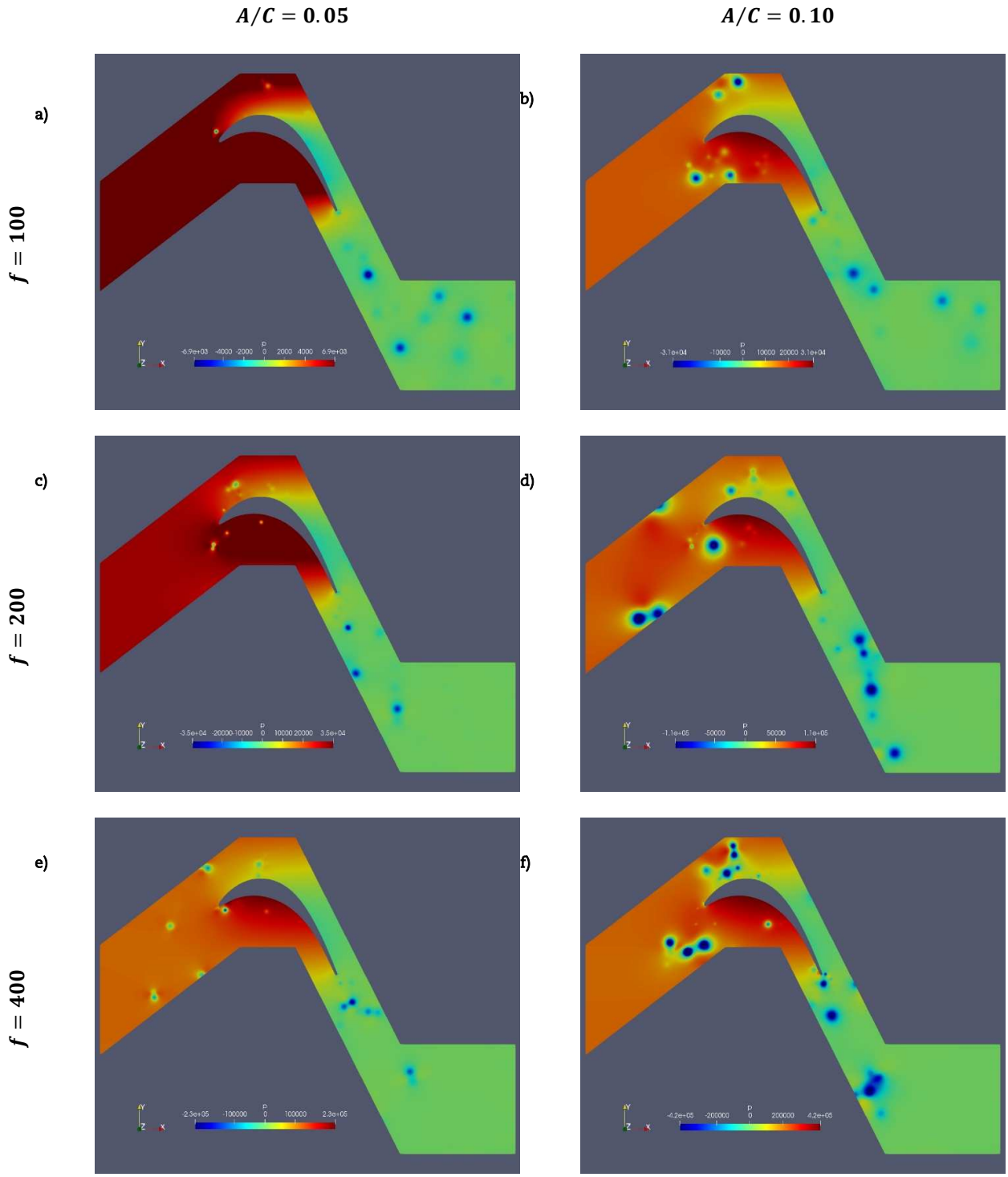

Fig. 6(i). Instantaneous pressure fields for a single vibrating T106A blade with $Re = 8000$ for the cases (left to right) $A/C = 0.05,0.10$ and (top to bottom) $f = 100,200,400$.

Figure 7 shows the variation of pressure over the surface of the vibrating blades for all cases considered here. The data for this figure is that which was produced after the entire simulation time had elapsed. It is apparent from comparing the first (stationary case) and subsequent (vibrating cases) rows of Fig. 7 that the effect of the vibrations is significant for all but the smallest amplitudes and frequencies and that even the most modest changes in either can lead to significant differences in both the shape and magnitude of the pressure profile. More specifically, it is apparent that an increase in the amplitude of the vibration leads to a significant increase in the magnitude of the pressure on the whole length of the lower, pressure surface of the blade, with the magnitude of the change increasing with increasing frequency. There is, however, a lesser, but nonetheless noticeable, change in the pressure on the suction surface of the blade, such that the change varies along the length of the blade: the leading edge undergoes an increase in the pressure, but the trailing edge undergoes a decrease in pressure. The magnitude of the change increases with increasing frequency and also the location on the suction surface at which the increase/decrease switch takes place moves closer towards the trailing edge with increasing frequency. The same pattern can be observed for the higher amplitude vibrations (Fig. 7, bottom row). However, in these cases, for the highest amplitudes (A/C=0.05,0.10) there is an onset of fluctuations in the pressure profile, especially along the suction surface of the blade. The fluctuations increase both with increasing amplitude and frequency.

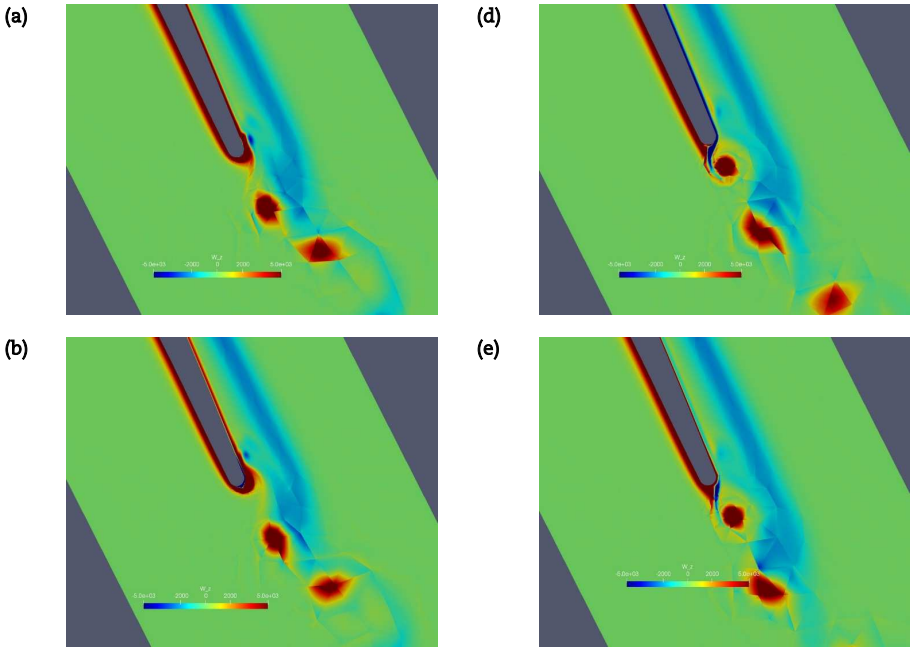

Fig 6(ii). Evolution of instantaneous vorticity fields for a single vibrating T106A blade with $Re = 8000$ for the case $A/C = 0.005$ and $f = 400$ at times (a-e) $\omega t = 0.4\pi, 0.8\pi, 1.2\pi, 1.6\pi, 2.0\pi$.

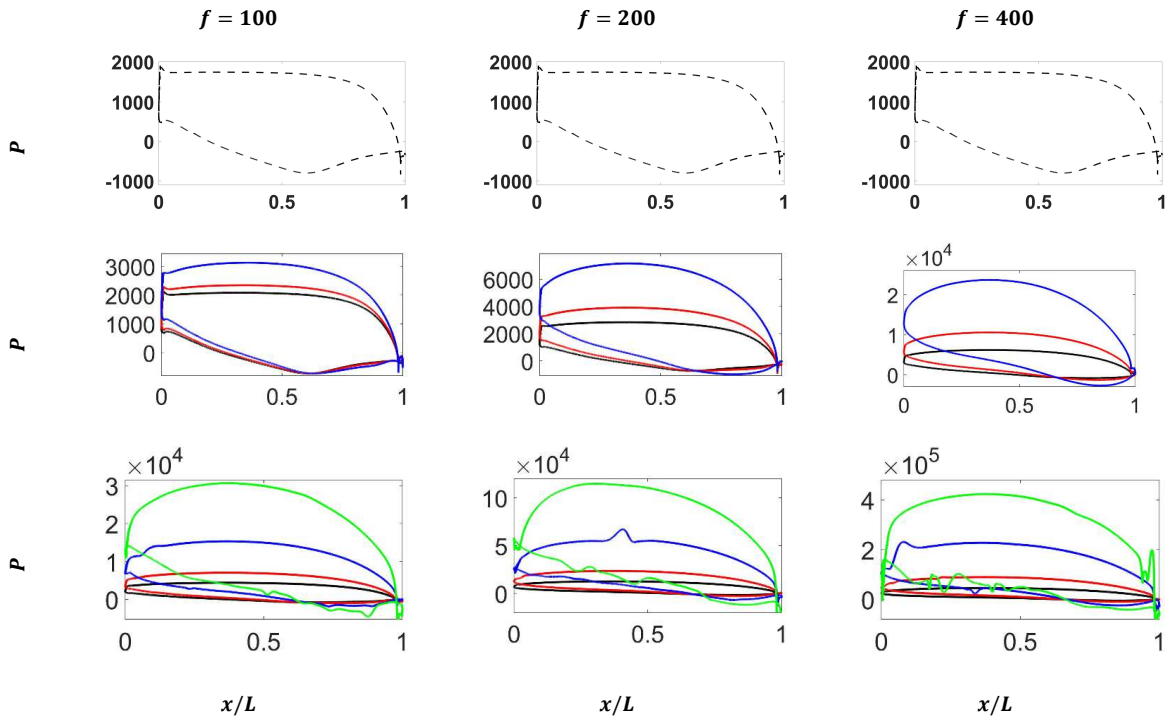

Fig. 7. Variation of pressure, P, over the surface of stationary and vibrating T106A blades with $Re = 8000$ for the cases with frequencies (left to right) $f = 100,200,400$ and amplitudes: (first row) $A/C = 0.000$ (black, dashed) , (second row) $A/C = 0.001,0.002,0.005$ (black-red-blue) and (third row) $A/C = 0.01,0.02,0.05,0.10$ (black-red-blue-green).

In order to evaluate the mean and fluctuating components (i.e. components arising due to the mean flow and due to the vibrations respectively) of the pressure independently around the blade, 3 sets of data taken during the final time period of vibration are considered. Fig. 8 shows the mean pressure component, $\bar{P}$ and the fluctuating components, $\tilde{P}_A$, and $\tilde{P}_B$ for all cases considered here. The information conveyed by this figure with regard to the mean component and the total fluctuating component reinforces that which was already observed in Fig. 7. Namely, that only for smallest amplitudes and lowest frequency vibrations (i.e. A/C=0.001,0.002 and f=100) can the fluctuating component be considered negligible in comparison to the mean component. In a further number of limited cases (i.e. A/C=0.005 and f=100, A/C=0.001,0.002 and f=200) these components can be considered to be of similar importance. However, a further increase of either parameter leads to the development of significant further differences, such that the mean component becomes negligible in comparison to the component arising due to the vibrations. It is also noteworthy that the total fluctuating component on the whole follows closely the first and not the second fluctuating component. $\tilde{P}_B$ remains negligible for most cases along most of the length of both surfaces of the blade. A few notable exceptions are visible where $\tilde{P}_B$ assumes non-negligible values. However, these often serve merely to strengthen fluctuations in the total fluctuating component (e.g. for f=400 and A/C=0.05 at low value of x/L). The fluctuations observed in the profile of pressure in Fig. 7 for higher amplitude vibrations are equally noticeable in the components of P for the same amplitudes and can be seen to be a feature of all components of the pressure.

The variation of the pressure phase angle, $\tan(\phi_P) = \tilde{P}_A / \tilde{P}_B$ such that $-\pi/2 < \phi_P < \pi/2$, along the blade is shown in Fig. 9. The parameter ϕ_P assumes values close to $\pm\pi/2$ when pressure ratio is of large magnitude, which occurs often due to the behavior of the pressure fluctuations (see Fig. 8). Furthermore, discontinuities occur as $\tilde{P}_B$ drops or rises through zero. Such discontinuities are therefore more common for higher amplitude and higher frequency vibrations, where the sign of $\tilde{P}_B$ changes frequently (as seen in Fig. 8). However, for lower amplitudes (A/C≤0.05) a pattern develops: at low frequency the parameter $\phi_P \leq -\pi/4$, which tends to $-\pi/2$ as the frequency increases. In addition, there exists a discontinuity in the region of $x/L \approx 0.7$ at all frequencies and at all amplitudes, and the gradient of ϕ_P in the vicinity of this discontinuity becomes increasingly steep as the frequency increases. This feature of the data is more readily apparent from the scatter plots of the manipulated data, which show the variation of the pressure phase angle along the blade. This particular discontinuity corresponds, not to minor oscillations due to the fluctuations, but to a clearly apparent (see Fig. 8) switch over in sign as of $\tilde{P}_A$ drops below zero and $\tilde{P}_B$ rises above zero along the suction surface of the blade as the trailing edge is approached.

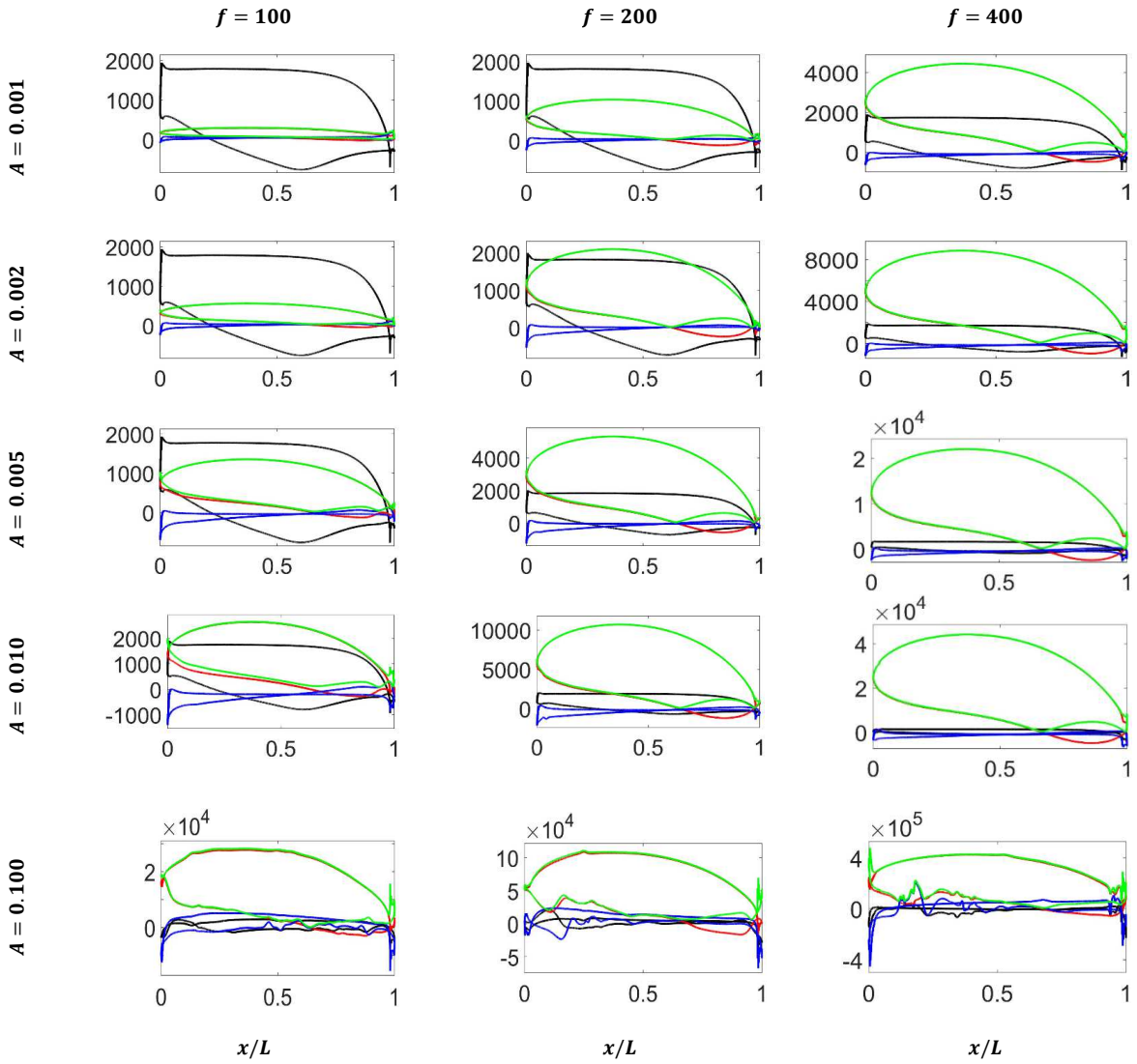

Fig. 8. Variation of pressure components, (black-red-blue-green) $\bar{P}, \tilde{P}_A, \tilde{P}_B, \tilde{P}$, over the surface of a vibrating T106A blade with $Re = 8000$ for the cases with frequencies (left to right) $f = 100,200,400$ and amplitudes (top to bottom)

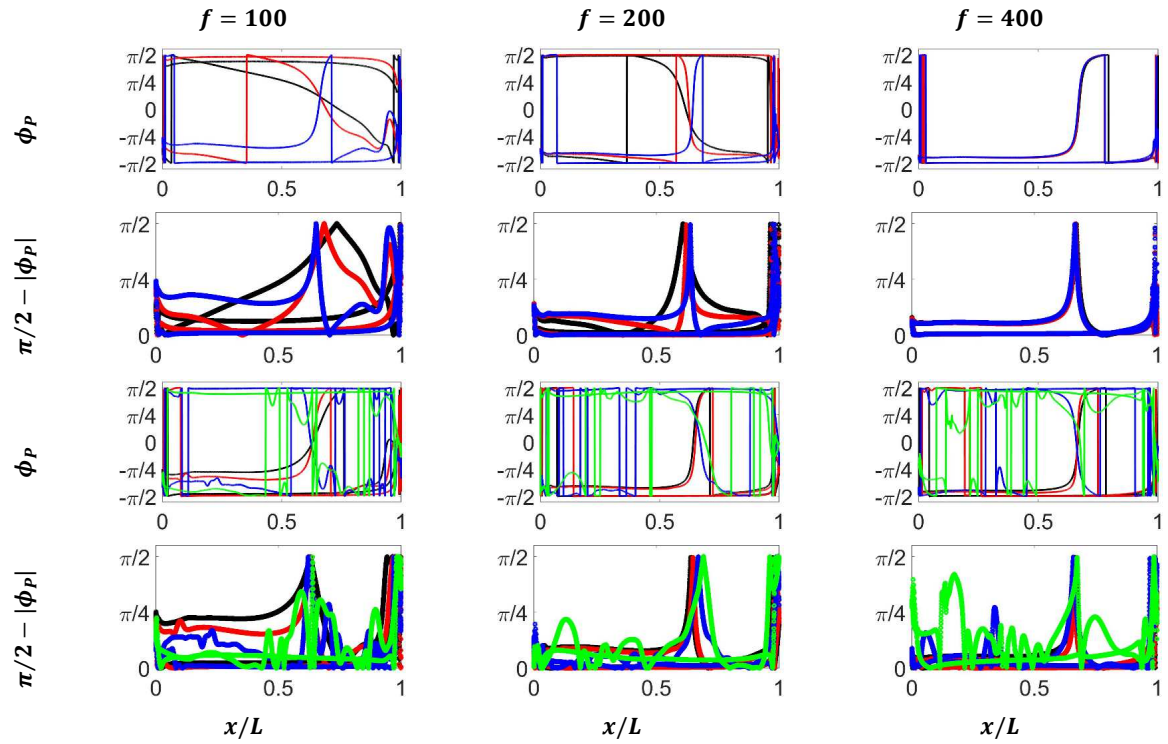

Fig. 9. (Rows 1,3) Variation of pressure phase angle, ϕ_P, and (rows 2,4) scatter plot of $\pi/2 - |\phi_P|$ over the surface of a vibrating T106A blade with $Re = 8000$ for the cases with frequencies (left to right) $f = 100,200,400$ and amplitudes (rows 1-2) $A/C = 0.001,0.002,0.005$ (black-red-blue) and (rows 3-4) $A/C = 0.01,0.02,0.05,0.10$ (black-red-blue-green).

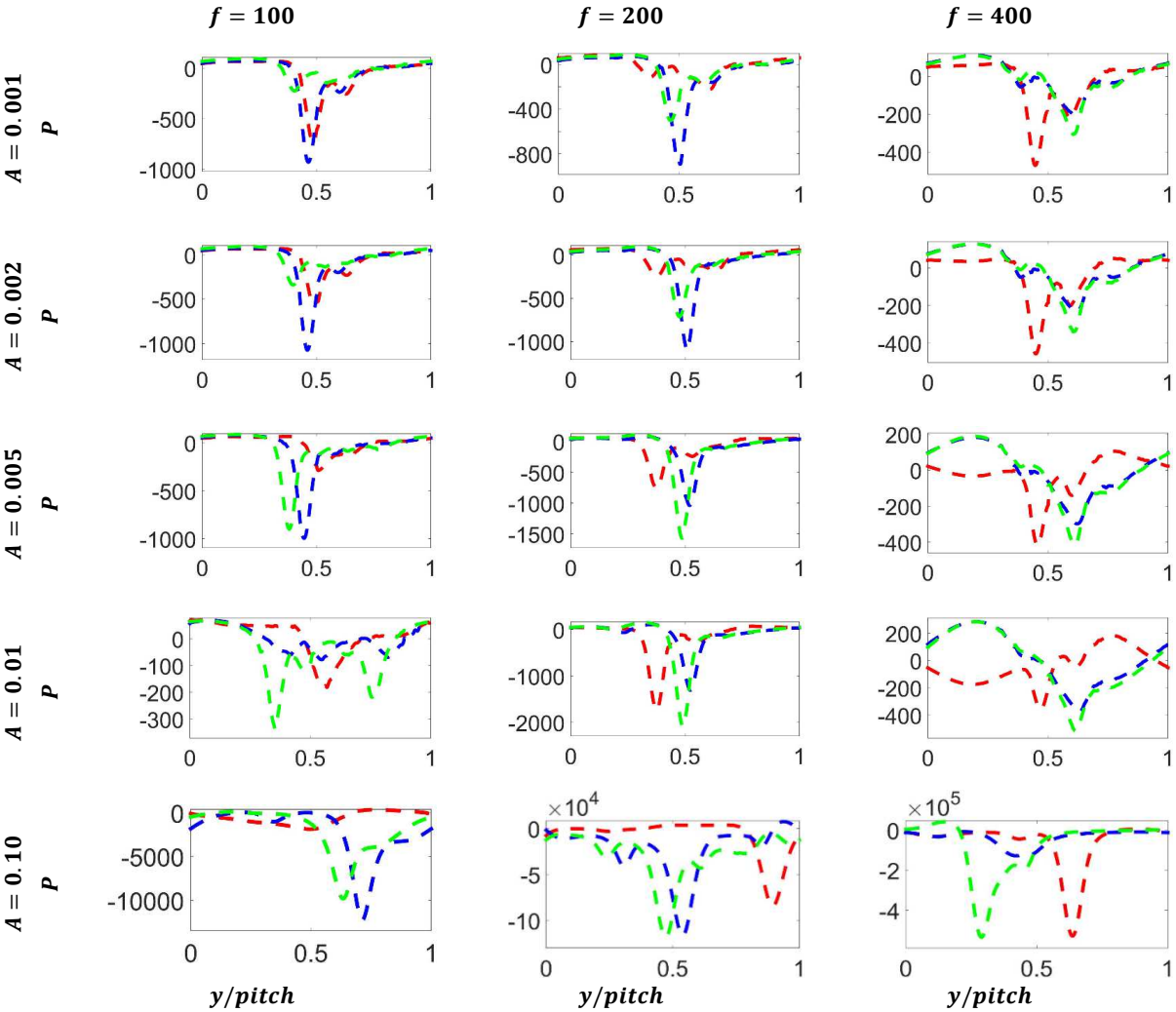

Fig. 10(i). Variation in pitch direction of pressure wake $0.35C$ downstream of trailing edge at times (red-blue-green) $\omega t = \pi, 1.8\pi, 2\pi$ of a vibrating T106A blade with $Re = 8000$ for the cases with frequencies (left to right) $f = 100,200,400$ and amplitudes (top to bottom)

As in the case of the stationary blade, the wake loss has been evaluated at a position 0.35C downstream (in the x-direction) of the trailing edge of the blade, henceforth referred to as the 'wake loss position'. The total wake loss can be decomposed into components which arise due to the mean flow and due to the vibrating motion of the blade. To this end, the same 3-time reference points that were utilized to evaluate the pressure components (i.e. ωt=π,1.8π,2π) were again utilized to evaluate the wake loss components. Fig. 10 shows the variation of the total pressure at both (Fig. 10(i)) the inlet and (Fig. 10(ii)) the wake loss position at these 3 times. It is of considerable importance to notice that the inlet pressure, although not varying significantly across the inlet, varies considerably with time, whereas the total pressure at the wake loss position exhibits the opposite dependence. Furthermore, for low amplitude and low frequency the inlet pressure at the bottom of the blade's oscillation (ωt=π) is strongly positive, but as either amplitude or frequency increase the inlet pressure becomes strongly negative. In contrast the inlet pressure at or near the top of the blade's oscillation (ωt=1.8π,2π) is strongly positive. Most inlet pressures, with the exception of cases for which the inlet pressure at the bottom of the blade's oscillation (ωt=π) is transitioning through zero, are of similar order of magnitude, in contrast to the lower order of magnitude at the wake loss position, with the exception of where the wake loss position coincides with a vortical structure. Although both the magnitude of the total pressure at the inlet and the magnitude of the total pressure inside the vortical structures at the wake loss position increase with increasing vibration amplitude and/or frequency, the magnitude of the vortical structures increases at the higher rate. Fig. 11 shows the total wake loss at the three time instants, which once more emphasizes the dependence of this parameter on the location of the blade in its oscillation: the total wake 'loss' represents a total wake 'gain' ($-w_e$ is negative) when the blade is at the lowest point in its oscillation. The magnitude of $-w_e$ increases with increasing vibration amplitude and frequency.

The mean, and fluctuating components of the wake loss are shown in Fig. 12 for all cases considered here. As was observed with regard to the pressure (see Fig. 8), the most significant component in most cases is the fluctuation in A direction, which dominates over B in the evaluation of the mean vorticity. The magnitude of the dominant component(s) increase(s) with increasing vibration amplitude and/or frequency and remains positive throughout all cases with almost no exceptions. The magnitude of fluctuations remains close to zero in all cases, except for a number of fluctuations which correspond to the location of vortical structures at the wake loss position. As a result of the negligible values which $\tilde{w}_{eB}$ attains and the dominant and positive nature of $\tilde{w}_{eA}$ the wake loss phase angle, ϕ_{we}, assumes values close to $\pm\pi/2$ for most parameter values considered here. The plots of this parameter are shown in Fig. 13 and the most noticeable exceptions occur for the largest amplitude vibrations (i.e. A/C=0.10) where the magnitude of $\tilde{w}_{eB}$ becomes comparable to that of $\tilde{w}_{eA}$ in the vicinity of large vortical structures. This behavior is amplified by increasing frequency.

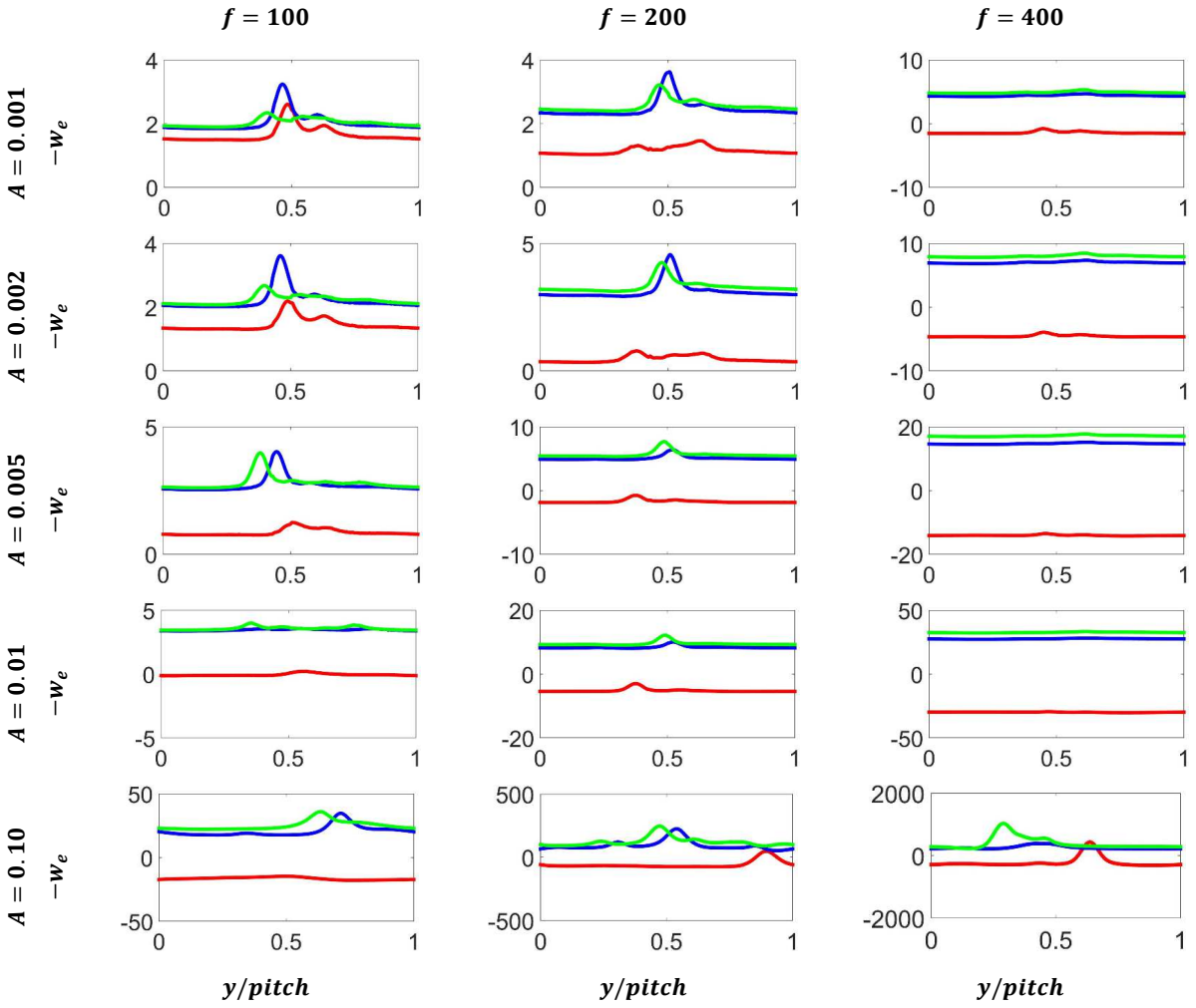

Fig. 11. Variation in pitch direction of wake loss, w_e, $0.35C$ downstream of trailing edge at times (red-blue-green) $\omega t = \pi, 1.8\pi, 2\pi$ of a vibrating T106A blade with $Re = 8000$ for the cases with frequencies (left to right) $f = 100,200,400$ and amplitudes (top to bottom)

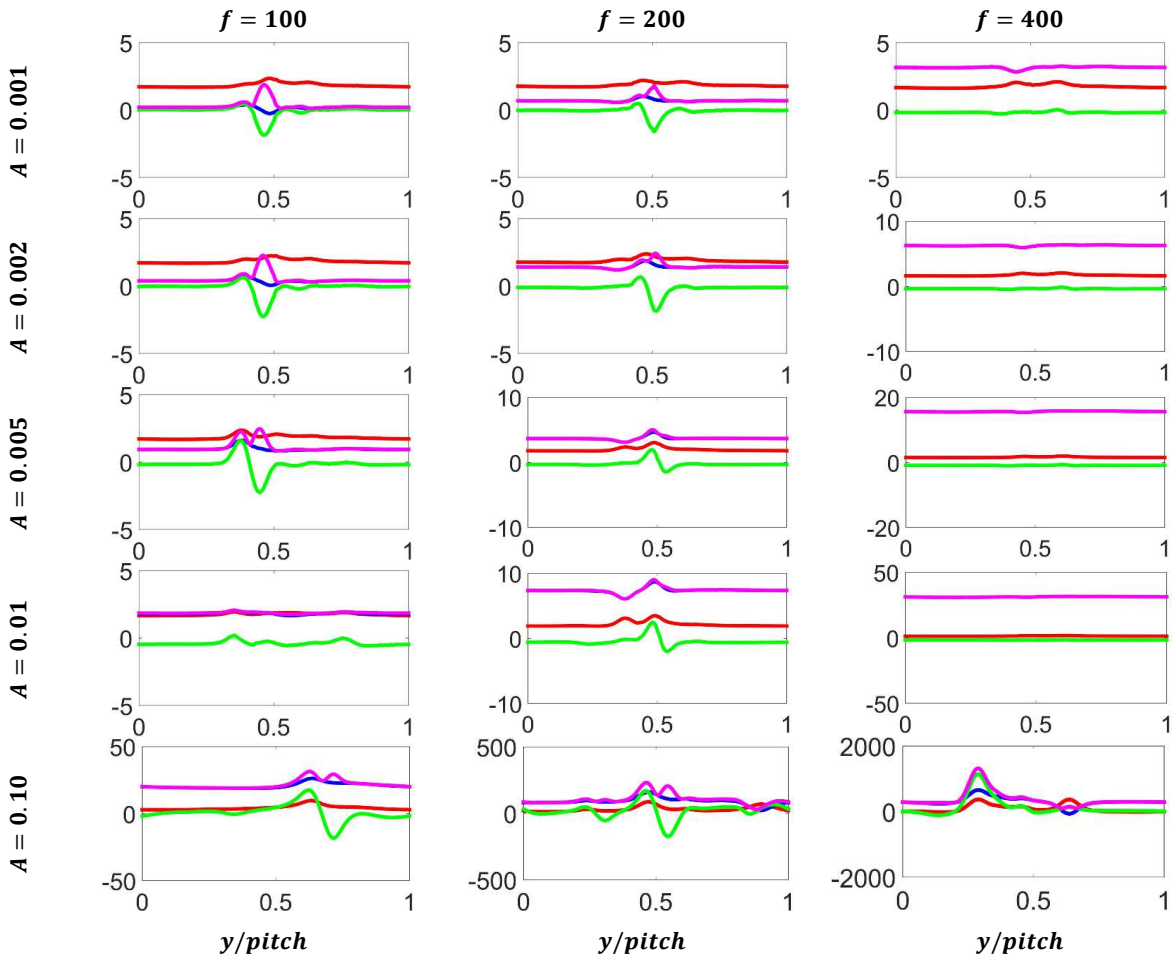

Fig. 12. Variation in pitch direction of components of wake loss (red-blue-green-magenta), $-(\widetilde{w_e}), -(\widetilde{w_e})_A, -(\widetilde{w_e})_B, (\widetilde{w_e})$, $0.35C$ downstream of trailing edge of a vibrating T106A blade with $Re = 8000$ for the cases with frequencies (left to right) $f = 100,200,400$ and amplitudes (top to bottom).

5. Conclusion

The Spectral/HP element method has been applied to perform DNS over a single T106A turbine blade-row using Nektar++'s incompressible flow solver for the 2D Navier-Stokes equations. The blades were subjected to one dimensional, pitch-wise forced-response harmonic vibrations and the effect on the resulting flow field was studied parametrically with respect to the amplitude and frequency of the vibrations. The pressure and vorticity fields showed the presence of vortical structures which had developed in the vicinity of both the leading and trailing edges. Under sufficiently large amplitude and frequency the vortical structures associated with the leading edge were seen to travel upstream, affecting the flow's behavior between the inlet and the leading edge. It was shown that on the blade surface the vibration-induced pressure component, $\tilde{P}$, played the most significant role in all but the smallest amplitude vibrations, and that the behavior of $\tilde{P}$ itself followed closely that of $\tilde{P}_A$ (as opposed to $\tilde{P}_B$). Increases in vibration amplitude and/or pressure resulted in an even stronger $\tilde{P}_A$ dominance but were accompanied by fluctuations in the pressure profile along the suction surface. The pressure field in the vicinity of the inlet and, consequently, the wake loss was shown to be strongly affected by the vibrations and in particular by the position of the blade in its oscillation. A breakdown of the wake loss into its components revealed a similar trend to that observed around the blade, namely that it was dominated by the vibration induced component $\tilde{w}_e$, or more specifically, by $\tilde{w}_{eA}$. Further analysis is now required in order to explain the underlying physical reasons that lead small-amplitude vibrations to dominate over the mean flow-field effects.

Author Contributions

D.H. Wacks performed simulations and wrote the manuscript; M.E. Nakhchi modified the manuscript, improved the quality and structure of the manuscript; M. Rahmati supervised the project and proofread the manuscript.

Acknowledgments

The authors would like to acknowledge the financial support received from Engineering Physics and Science Research Council of UK (EPSRC EP/R010633/1).

Conflict of Interest

The authors declared no potential conflicts of interest with respect to the research, authorship, and publication of this article.

References

[1] Stieger, R., Hollis, D., and Hodson, H., Unsteady surface pressures due to wake-induced transition in a laminar separation bubble on a low-pressure cascade, *Journal of Turbomachinery*, 126 (4), 2004, 544-550.
[2] Himmel, C. G., *Ultra-high lift blades for low pressure turbines*, University of Cambridge, 2010.
[3] Hodson, H. P., and Howell, R. J., Bladerow interactions, transition, and high-lift aerofoils in low-pressure turbines, *Annual Review of Fluid Mechanics*, 37, 2005, 71-98.
[4] D Coull, J., and Hodson, H. P., Unsteady boundary-layer transition in low-pressure turbines, *Journal of Fluid Mechanics*, 681, 2011, 370.
[5] Panovsky, J., and Kielb, R. E., A design method to prevent low pressure turbine blade flutter, *Journal of Engineering for Gas Turbines and Power*, 122(1), 2000, 89-98.
[6] Waite, J. J., and Kielb, R. E., Physical understanding and sensitivities of low pressure turbine flutter, *Journal of Engineering for Gas Turbines and Power*, 137(1), 2015, 012502.
[7] Izadpanah, E., Yazdanian, M., Hekmat, M. H., and Amini, Y., Thermal Performance of Oscillating Blade with Various Geometries in a Straight Channel, *Journal of Applied and Computational Mechanics* (Articles in Press), 2020.
[8] Rinne, E., Holttinen, H., Kiviluoma, J., and Rissanen, S., Effects of turbine technology and land use on wind power resource potential, *Nature Energy*, 3(6), 2018, 494-500.
[9] Hong, J., Toloui, M., Chamorro, L. P., Guala, M., Howard, K., Riley, S., Tucker, J., and Sotiropoulos, F., Natural snowfall reveals large-scale flow structures in the wake of a 2.5-MW wind turbine, *Nature Communications*, 5, 2014, 4216.
[10] Strom, B., Brunton, S. L., and Polagye, B., Intracycle angular velocity control of cross-flow turbines, *Nature Energy*, 2(8), 2017, 1-9.
[11] Dowell, E. H., Curtiss, H. C., Scanlan, R. H., and Sisto, F., *A modern course in aeroelasticity*, Springer, 1989.
[12] Besem, F. M., Kielb, R. E., Galpin, P., Zori, L., and Key, N. L., Mistuned forced response predictions of an embedded rotor in a multistage compressor, *Journal of Turbomachinery*, 138(6), 2016, 061003.
[13] Silkowski, P. D., and Hall, K. C., *A coupled mode analysis of unsteady multistage flows in turbomachinery*, ASME 1997 International Gas Turbine and Aeroengine Congress and Exhibition, June 2–5, Orlando, Florida, USA, 1997.
[14] Shams, S., Molaei, A., and Mirzavand, B., Torsional Aeroelasticity of a Flexible VAWT Blade using a Combined Aerodynamic Method by Considering Post-stall and Local Reynolds Regime, *Journal of Applied and Computational Mechanics*, 6(4), 2020, 757-776.
[15] Hatami, M., Cuijpers, M., and Boot, M., Experimental optimization of the vanes geometry for a variable geometry turbocharger (VGT) using a Design of Experiment (DoE) approach, *Energy Conversion and Management*, 106, 2015, 1057-1070.
[16] Jafaryar, M., Kamrani, R., Gorji-Bandpy, M., Hatami, M., and Ganji, D., Numerical optimization of the asymmetric blades mounted on a vertical axis cross-flow wind turbine, *International Communications in Heat and Mass Transfer*, 70, 2016, 93-104.
[17] Bovand, M., Rashidi, S., Esfahani, J., and Masoodi, R., Control of wake destructive behavior for different bluff bodies in channel flow by magnetohydrodynamics, *The European Physical Journal Plus*, 131(6), 2016, 194.
[18] Rashidi, S., Bovand, M., Esfahani, J., Öztop, H., and Masoodi, R., Control of wake structure behind a square cylinder by magnetohydrodynamics, *Journal of Fluids Engineering*, 137(6), 2015, 061102.
[19] Rashidi, S., Hayatdavoodi, M., and Esfahani, J. A., Vortex shedding suppression and wake control: A review, *Ocean Engineering*, 126, 2016, 57-80.
[20] Rashidi, S., Bovand, M., and Esfahani, J. A., Application of magnetohydrodynamics for suppressing the fluctuations in the unsteady flow around two side-by-side circular obstacles, *The European Physical Journal Plus*, 131(12), 2016, 1-12.
[21] Hall, K. C., Thomas, J. P., and Clark, W. S., Computation of unsteady nonlinear flows in cascades using a harmonic balance technique, *AIAA Journal*, 40(5), 2002, 879-886.
[22] Rahmati, M., He, L., and Li, Y., The blade profile orientations effects on the aeromechanics of multirow turbomachines, *Journal of Engineering for Gas Turbines and Power*, 138(6), 2016, 062606.
[23] Rahmati, M., He, L., Wang, D., Li, Y., Wells, R., and Krishnababu, S., Nonlinear time and frequency domain methods for multirow aeromechanical analysis, *Journal of Turbomachinery*, 136(4), 2014, 041010.
[24] Rahmati, M., He, L., and Wells, R., *Interface treatment for harmonic solution in multi-row aeromechanic analysis*, ASME Turbo Expo 2010: Power for Land, Sea, and Air, June 14–18, Glasgow, UK, 2010.
[25] Michelassi, V., Chen, L.-W., Pichler, R., and Sandberg, R. D., Compressible Direct Numerical Simulation of Low-Pressure Turbines—Part II: Effect of Inflow Disturbances, *Journal of Turbomachinery*, 137(7), 2015, 071005.
[26] Wissink, J., DNS of separating, low Reynolds number flow in a turbine cascade with incoming wakes, *International Journal of Heat and Fluid Flow*, 24(4), 2003, 626-635.
[27] Garai, A., Diosady, L. T., Murman, S. M., and Madavan, N. K., *DNS of low-pressure turbine cascade flows with elevated inflow turbulence using a discontinuous-Galerkin spectral-element method*, ASME Turbo Expo 2016: Turbomachinery Technical Conference and Exposition, June 13–17, Seoul, South Korea, 2016.
[28] Nakhchi, M. E., Naung, S. W., and Rahmati, M., DNS of secondary flows over oscillating low-pressure turbine using spectral/hp element method, *International Journal of Heat and Fluid Flow*, 86, 2020, 108684.
[29] Cantwell, C. D., Moxey, D., Comerford, A., Bolis, A., Rocco, G., Mengaldo, G., De Grazia, D., Yakovlev, S., Lombard, J.-E., and Ekelschot, D., Nektar++: An open-source spectral/hp element framework, *Computer Physics Communications*, 192, 2015, 205-219.
[30] Moxey, D., Cantwell, C. D., Bao, Y., Cassinelli, A., Castiglioni, G., Chun, S., Juda, E., Kazemi, E., Lackhove, K., and Marcon, J., Nektar++: Enhancing the capability and application of high-fidelity spectral/hp element methods, *Computer Physics Communications*, 249, 2020, 107110.
[31] Bao, Y., Palacios, R., Graham, M., and Sherwin, S., Generalized thick strip modelling for vortex-induced vibration of long flexible cylinders, *Journal of Computational Physics*, 321, 2016, 1079-1097.
[32] Bao, Y., Zhu, H., Huan, P., Wang, R., Zhou, D., Han, Z., Palacios, R., Graham, M., and Sherwin, S., Numerical prediction of vortex-induced vibration of flexible riser with thick strip method, *Journal of Fluids and Structures*, 89, 2019, 166-173.

ORCID iD

Daniel H. Wacks https://orcid.org/0000-0002-3985-9344
M. E. Nakhchi https://orcid.org/0000-0003-1034-6091
M. Rahmati https://orcid.org/0000-0003-4903-5370

How to cite this article: Wacks D.H., Nakhchi M.E., Rahmati M. Forced Response of a Low-Pressure Turbine Blade using Spectral/hp Element Method: Direct Numerical Simulation, *J. Appl. Comput. Mech.*, 7(1), 2021, 135–147. https://doi.org/10.22055/JACM.2020.34843.2480